Available online at www.sciencedirect.com
ScienceDirect
Journal of Nuclear Materials 362 (2007) 316–326
journal of nuclear materials
www.elsevier.com/locate/jnucmat

Variable incidence angle – X-ray absorption spectroscopy for the study of Zircaloy corrosion layers

Claude Degueldre [a,*], Michael Kastoryano [a], Kathy Dardenne [b]

[a] NES, Paul Scherrer Institute, 5232 Villigen, Switzerland
[b] INE, Forschungszentrum Karlsruhe, 76021 Karlsruhe, Germany

Abstract

Variable incidence angle X-ray absorption fine structure (VIAXAFS) spectroscopy has been used for its non-destructive ability to probe and investigate nano-structures in zirconia films. The theory of X-ray absorption–detection in fluorescence mode was revisited and applied to the variable incidence angles of the photon beam for studying a corrosion film. The expression derived for the depth profile was used to evaluate nano-structures and atom environments in the film. This technique was applied, spanning angles from a grazing towards normal incidence on a sample layer obtained by zirconium alloy corrosion. XAFS analysis on the Zr K edge suggests a lower number of next neighbour Zr atoms in the corroded samples. This may be due to the relative density for given average atom distances suggesting a high density of dislocations and defects. The discussion underlines that the technique reveals nano-pores, dislocations, vacancies or defect features. The presence of tetragonal zirconia is not observed for zirconium alloy corrosion layers.

PACS: 61.10.Ht; 68.47.Gh; 78.66.−W

1. Introduction

The purpose of these X-ray absorption fine structure (XAFS) investigations is first to contribute to the study of corrosion layers in a non-destructive way. In the theoretical Section the mathematics underlying the described variable incidence angle X-ray absorption fine structure (VIAXAFS) methodology is summarized. The mathematical analysis is inspired from previous work on self-absorption correction by Booth et al. [1], Pfalzer et al. [2] and Tröger et al. [3]. Although the formalism yields a nearly exact algorithm for subtracting surface layers and isolating deep layers, in practice there are several simplifying assumptions that have to be made in order to come up with a result that adequately reflects the experimental data.

The theory of absorption spectroscopy in fluorescence mode was revised and applied to the variable incidence angles of the photon beam (for more details see [4]). An expression is derived for the depth profile evaluation for nano-structures, and atom environment. This technique was applied, spanning angles from a grazing to normal incidence on a sample layers obtained by zirconium alloy corrosion.

* Corresponding author. Tel.: + 41 56 3104176; fax: + 41 56 3103565.
E-mail address: claude.degueldre@psi.ch (C. Degueldre).

0022-3115/$ - see front matter © 2007 Elsevier B.V. All rights reserved.
doi:10.1016/j.jnucmat.2007.01.233

Zirconia, which is currently used as coating, is also a corrosion product of zirconium alloys e.g. Zircaloy (Zry). Zirconia layers act as Zry passive film, and their properties with regard to the transport of water-derived species or energy are of safety relevance in several applications e.g. [5]. However, the thermal conductivity of a zirconia layer is driven by phonon transport, which is primarily a function of varying pore and defect densities in the film [6]. This renders the study of zirconia layers of great interest in nuclear safety and other sciences, particularly with regard to its behaviour at the atomic level.

The zirconia films may include distortions, dislocations and/or nano-pores, which modify the Zr environment. The influence of oxygen deficiency on the electronic and on local structure of monoclinic zirconia has recently been examined and compared to a cubic stabilized sample in XAFS studies e.g. [7,8]. In this study VIAXAFS has been applied to a zirconia layer obtained by Zry corrosion, completing a recent study of zirconia films by grazing incidence (GI)XAFS [9].

2. Theoretical background

The mathematical analysis is inspired from previous work on self-absorption correction by Booth et al. [1], and Tröger et al. [3]. Although the formalism yields a nearly exact algorithm for subtracting surface layers and isolating deep layers, in practice there are several simplifying assumptions that have to be made in order to come up with a result that adequately reflects the experimental data.

First, a general expression is obtained for the fluorescence yield intensity reaching the detector for a given ample and incidence angle. The experimental normalized absorption factor (χ) for the target region was then derived as a function of the χ-data from the spectra of the two successive angles spanning the target region and additionally [1] the self-absorption was accounted for a quasi-exact formulation of the χ-factor from the experimental data.

The fluorescence yield intensity (I_f) is obtained by summing all fluorescence photons generated along the penetration path of the incident X-ray beam, as shown in Fig. 1. The penetration pathway of the incoming beam follows an inverse exponential law known as Lambert's law, with I_0 the incoming beam intensity undergoing absorption with $\mu_T(E)$ the energy (E) dependant coefficient of absorption, and l_i is the penetration depth. An absorbing atom in the material will reemit a photon of energy E_f with a probability $\varepsilon_a(E)$, dependant on the sample material. In order to detect the reemitted photon with the fluorescence detector, it must first travel back through the material to the surface interface. Along this second path (l_f), it will be absorbed with a probability following Lambert's law but with a different coefficient of absorption $\mu_T(E_f)$, where E_f is the energy of fluorescence of the material. The fluorescence flux at the detector from the point of absorption, approximated by an infinitesimal line element in the sample, can then be expressed as follows:

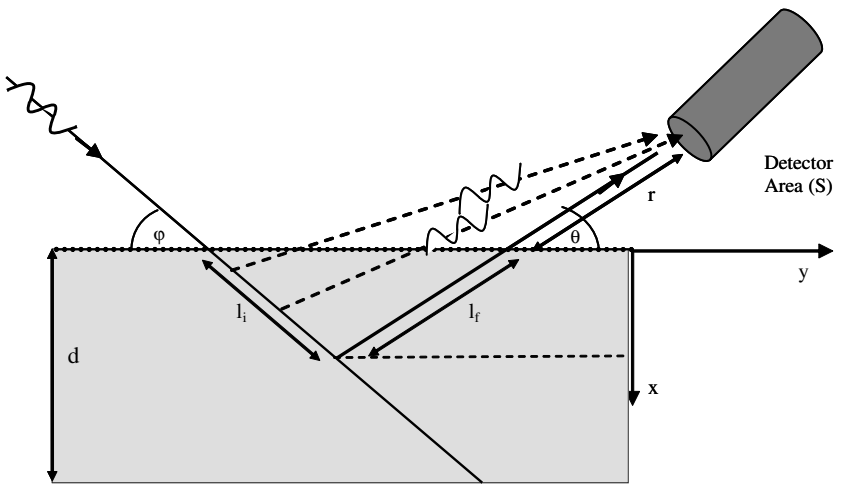

Fig. 1. VIAXAFS geometry of setup. The incoming beam is attenuated as it enters the material until its reemission spectrum becomes imperceptibly weak.

$$dI_f = \frac{S}{r^2} I_0 \varepsilon_a \mu_a e^{-(\mu_T l_i + \mu_f l_f)} dl_i, \quad (1)$$

where S/r^2 is the solid angle subtended by the detector surface S, $\mu_a(E)$ is the absorption coefficient due to the core hole creation process of the absorbing atom's target shell. Note that the reemission can reasonably be considered a one dimensional process as long as $r^2 \gg S$, and $r \gg l_f$. It must also be noted that $E_f < E$ for the edge energy of the element under study, and that in general $\mu(E_f) < \mu(E)$; as long as the studied element is lighter than the crystal structure matrix. Simplifying the absorption coefficient symbols using $\mu_T = \mu_T(E)$ and $\mu_f = \mu_T(E_f)$, and letting the variables l_i and l_f be expressed in terms of x as $x = l_i \sin\varphi$ and $x = l_0 \sin\theta$, and assuming that all the measured fluorescence is coming from the desired process, Eq. (2) becomes

$$dI_f = \frac{S}{r^2} I_0 \varepsilon_a \mu_a \frac{1}{\sin\varphi} e^{-\left(\frac{\mu_T}{\sin\varphi} + \frac{\mu_f}{\sin\theta}\right)x} dx. \quad (2)$$

Integrating over x from the sample interface to the peak depth d yields:

$$I_f = \frac{S}{r^2} I_0 \varepsilon_a \frac{\mu_a}{\mu_T + g\mu_f} \left[e^{-\left(\frac{\mu_T}{\sin\varphi} + \frac{\mu_f}{\sin\theta}\right)d} - 1 \right], \quad (3)$$

where $g \equiv \frac{\sin\varphi}{\sin\theta}$. Eq. (3) describes the total fluorescence intensity received at the detector for the given setup. It is important to note here that the integral evaluated in Eq. (3) is not strictly accurate in VIAXAFS, because in general the absorption coefficient is depth dependant, which modifies the evaluation of the integral. However, for samples that are not too severely inhomogeneous, the absorption coefficient can be replaced by a constant weighted average along the penetration depth.

The goal of the VIAXAFS method is to express the absorption spectrum as a function of the sample depth. The procedure consists of 'subtracting' from the spectrum of penetration depth $x + \Delta x$ the information from the spectrum of penetration depth x. The incoming X-ray beam being of constant intensity, its penetration depth is always the same on a given sample. The information depth, however, depends on the incidence angle. A spectrum taken at an angle $\phi = 10°$ will provide less information of the interior of the sample than a spectrum taken at $\phi = 45°$ [3]. It is critical to properly define the variables in the following derivation and identify them with their designated equivalents.

Consider the beam approaching the sample at two different 'successive' angles ϕ and $\phi + \Delta\phi$, the incident beam will then penetrate the sample at corresponding depths of x and $x + \Delta x$. Experimental data can be compiled for the $\vartheta(x + \Delta x, \phi + \Delta\phi)$ configuration as well as for the $\vartheta(x, \varphi)$ one. However, in order to subtract the information of a shallow layer from a deeper one, the penetration path has to be identical in order to preserve the right ratio of relative intensities. In other words, the structural information of the sample, contained in the normalized absorption (χ), at $\vartheta(x, \varphi + \Delta\phi)$ has to be subtracted from the structural information at $\vartheta(x + \Delta x, \phi + \Delta\phi)$. Thus, it is necessary to express the normalized spectrum at $\vartheta(x, \varphi + \Delta\phi)$ in terms of the normalized spectrum at $\vartheta(x, \varphi)$. The correlation factor, denoted κ, is the quotient of the intensities.

The two measured intensities are given by

$$I_{x+\Delta x}^{\varphi+\Delta\varphi} \equiv \frac{S}{r^2} \varepsilon_a I_0 \frac{\mu_a^{x+\Delta x}}{\mu_T^{x+\Delta x} + g_{\varphi+\Delta\varphi}\mu_f^{x+\Delta x}} \times \left[e^{-(\mu_T^{x+\Delta x} + g_{\varphi+\Delta\varphi}\mu_f^{x+\Delta x})\frac{x+\Delta x}{\sin(\varphi+\Delta\varphi)}} - 1 \right],$$
$$I_x^{\varphi} \equiv \frac{S}{r^2} \varepsilon_a I_0 \frac{\mu_a^{x}}{\mu_T^{x} + g_{\varphi}\mu_f^{x}} \left[e^{-(\mu_T^{x} + g_{\varphi}\mu_f^{x})\frac{x}{\sin\varphi}} - 1 \right], \quad (4)$$

where the variables and constants are defined as in Eq. (4), and the subscripts and the superscripts designate the angles and penetration depths. Note that the absorption coefficients depend in fact only on the sample depth. The correlation coefficient is given by

$$\kappa_x \equiv \frac{I_x^{\varphi+\Delta\varphi}}{I_x^{\varphi}} = \frac{\mu_T^x + g_\varphi \mu_f^x}{\mu_T^x + g_{\varphi+\Delta\varphi}\mu_f^x} \frac{\left[e^{-(\mu_T^x + g_{\varphi+\Delta\varphi}\mu_f^x)\frac{x}{\sin(\varphi+\Delta\varphi)}} - 1 \right]}{\left[e^{-(\mu_T^x + g_\varphi \mu_f^x)\frac{x}{\sin\varphi}} - 1 \right]}, \quad (5)$$

from which the fluorescence yield intensity produced in the target region can then be expressed as

$$I(x, x + \Delta x) = I_{x+\Delta x}^{\varphi+\Delta\varphi} - I_x^{\varphi+\Delta\varphi} = I_{x+\Delta x}^{\varphi+\Delta\varphi} - \kappa_x I_x^{\varphi}. \quad (6)$$

The next logical step is then to rewrite Eq. (6) in a form that is computable. Consider the transformations relating the total absorption μ_T, the atomic absorption μ_z and the normalized absorption χ for the layers of depth x and $x + \Delta x$ and for the internal section $[x, x + \Delta x]$, with

$$\mu_{\mathrm{T}}^{x} = \bar{\mu}_{\mathrm{T}}^{x} + \chi_{x}^{\varphi}\bar{\mu}_{\mathrm{a}}^{x}, \quad \mu_{\mathrm{a}}^{x} = (\chi_{x}^{\varphi}+1)\bar{\mu}_{\mathrm{a}}^{x},$$
$$\mu_{\mathrm{T}}^{x} - \bar{\mu}_{\mathrm{T}}^{x} = \mu_{\mathrm{a}}^{x} - \mu_{\mathrm{a}}^{x},$$

where the overhead bars represent the corresponding spline functions of the variables.

As it was already indicated by Booth et al. [1] and suggested by Tröger et al. [3], the experimental value of the normalized absorption is not identical to the real value as in the transformation, but rather as $\chi_{\mathrm{exp}} = \frac{I_{\mathrm{f}} - I_{\mathrm{f}}}{I_{\mathrm{f}}}$.

The derivation of the real normalized absorption coefficient as a function of the experimental one, taking into consideration the self-absorption effect, is given in [1]. Using the transformations, the experimental normalized absorption can be expressed as

$$\chi_{\mathrm{exp}}^{\Delta} + 1 = \frac{I(x, x+\Delta x)}{\bar{I}(x, x+\Delta x)} = \frac{I_{x+\Delta x}^{\varphi+\Delta\varphi} - \kappa_x I_x^{\varphi}}{\bar{I}_{x+\Delta x}^{\varphi+\Delta\varphi} - \bar{\kappa}_x \bar{I}_x^{\varphi}},$$
$$\chi_{\mathrm{exp}}^{\Delta} + 1 = \frac{(\chi_{\mathrm{exp}}^{\varphi+\Delta\varphi}+1)\bar{I}_{x+\Delta x}^{\varphi+\Delta\varphi} - \kappa_x(\chi_{\mathrm{exp}}^{\varphi}+1)\bar{I}_x^{\varphi}}{\bar{I}_{x+\Delta x}^{\varphi+\Delta\varphi} - \bar{\kappa}_x \bar{I}_x^{\varphi}} \tag{7}$$

and the κ factor can be rewritten in terms of computable reference quantities as

$$\kappa_x = \frac{\chi_x^{\varphi}\bar{\mu}_{\mathrm{a}}^{x} + \bar{\mu}_{\mathrm{T}}^{x} + g_{\varphi}\mu_{\mathrm{f}}^{x}}{\chi_x^{\varphi}\bar{\mu}_{\mathrm{a}}^{x} + \bar{\mu}_{\mathrm{T}}^{x} + g_{\varphi+\Delta\varphi}\mu_{\mathrm{f}}^{x}} \times \frac{\left[\mathrm{e}^{-(\chi_x^{\varphi}\bar{\mu}_{\mathrm{a}}^{x} + \bar{\mu}_{\mathrm{T}}^{x} + g_{\varphi+\Delta\varphi}\mu_{\mathrm{f}}^{x})\frac{x}{\sin(\varphi+\Delta\varphi)}} - 1\right]}{\left[\mathrm{e}^{-(\chi_x^{\varphi}\bar{\mu}_{\mathrm{a}}^{x} + \bar{\mu}_{\mathrm{T}}^{x} + g_{\varphi}\mu_{\mathrm{f}}^{x})\frac{x}{\sin\varphi}} - 1\right]}. \tag{8}$$

But for reasonably small Δ, $\chi_{\mathrm{exp}}^{\Delta} \approx \chi_{\Delta}$, so Eq. (7) adequately expresses the normalized absorption coefficient for the region of depth $[x, x+\Delta x]$. Some caution has to be taken in analyzing the equations derived above. First of all, it has to be noted that the expressions for the various absorption coefficients are in fact averages. Therefore, if the absorption in the material changes rapidly with depth, then the variable angle step sizes have to be decreased, in which case the ratio of noise has to be closely studied in order to avoid false results. In a highly inhomogeneous sample it might also be very difficult to fit the intensity spline functions accurately. The χ-spectrum is a normalized EXAFS spectrum whose energy dependence is expressed in the transformed k scale using

$$k = \sqrt{2m_e/h^2(E - E_0)}. \tag{9}$$

They are further k weighted in order to let appear specific spectral features.

3. Experimental

3.1. Samples

The studied samples consisted of one pure Zr film for standardisation as well as several zirconia samples. As a reference, a ZrO_2 monoclinic powder (Fluka Proanalysis, monoclinic) was mixed with polyethylene (PE) and pressed into a pellet.

The film of the 10 μm ZrO_2/Zry sample was a 10 μm thick zirconia corrosion layer; it was produced by contacting a Zry sample with liquid water in an autoclave at 595 K under 15 MPa. Thickness was determined by gravimetry using a density of 5.8 g cm^{-3}; the porosity being believed to be of the order of 1–2%, a density correction is usually not required. By optical microscopy analysis, it was observed that the sample exhibits a flat surface coated with a fairly dense layer of asymmetric grains of size ~10 μm and spacing 2 μm. The SEM analysis confirms these observations. The roughness is assessed at ~3 μm (Fig. 2).

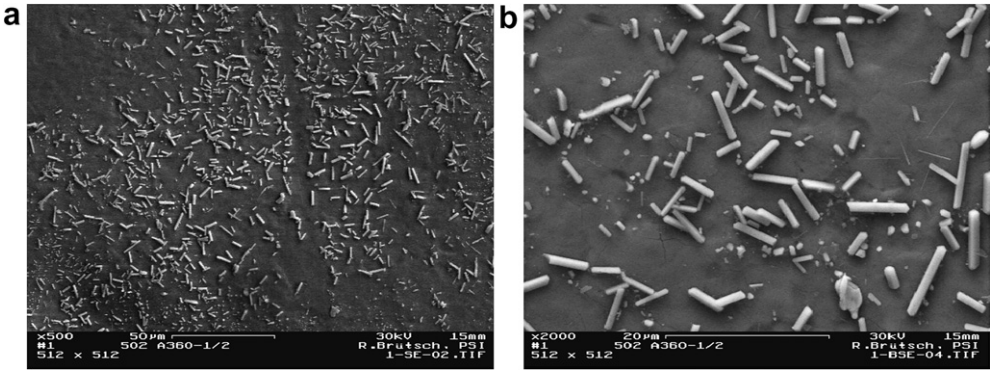

Fig. 2. (a) 10 μm ZrO_2/Zry sample, ×500 SEM zoom, 50 μm scale. (b) 10 μm ZrO_2/Zry sample, ×2000 SEM zoom, 20 μm scale.

3.2. XAFS

The Zr K X-ray absorption spectra were recorded at the INE beam line of the ANKA facility at the Forschungszentrum Karlsruhe, Germany. The ANKA storage ring was operated at 2.5 GeV electron energy with a mean electron current of 120 mA. The design of the beam line is multi-purposed, allowing for a number of different X-ray spectroscopic methods. VIAXAFS was applied on this facility because it completes the GIXAFS methodology applied on this line. The line uses a Lemonnier-type double crystal X-ray monochromator. The photon energies spanned by the monochromator range from ~2400 to ~24 000 eV, and the beam focus has roughly a 1 mm^2 cross section. The detector is a 5-pixel low energy fluorescence germanium solid state detector (Canberra–Packard Ultra-LEGe) capable as well of studying dilute samples and GIXAFS.

All measurements were recorded at room temperature. The reference sample spectrum was recorded in transmission mode while thin film samples spectra were taken in a grazing and variable incidence angle (GI–VIA) geometry with fluorescence detection mode. The different ZrO_2 thin films were measured without further preparation. Three Ar-filled ionization chambers at ambient pressure were used for simultaneous detection of the transmission signals of the ZrO_2 (monoclinic) sample and a Zr metal reference foil for energy calibration. The 1st ionization energy of Zr^0 (17 998 eV) [10] was taken at the first inflection point in the spectrum of Zr metal. Spectra were recorded at a 4 eV step-width in the pre-edge region (17 850–17 980 eV), 1 eV at the rising edge (17 981–18 100 eV), 2 eV above the edge (18 101–18 250 eV) and equidistant k-steps (0.04 $Å^{-1}$) in the EXAFS region (18 250–19 000 eV). The intensity of the monitor ionization chamber was held constant during each scan by means of a piezo-driven feedback to the second crystal (MOSTAB). The parallel alignment of the reflecting crystal faces was detuned to ~70% of the maximum beam intensity. In our set up, the fluorescence detection is orthogonal with the incident beam ($\phi + q = 90°$), and carried out with a 5-element solid-state Ge detector array cooled at 77 K.

3.3. FEFF

FEFF8 calculates extended X-ray absorption fine structure (EXAFS), X-ray absorption near edge structure (XANES), using an *ab initio* self-consistent real space multiple scattering approach for clusters of atoms, including polarization dependence. Calculations are based on an all-electrons real space relativistic Green's function formalism with no symmetry requirements. The method combines both full multiple scattering based on LU or Lanczos algorithms and a high-order path expansion based on the Rehr–Albers multiple scattering formalism. Calculations of the X-ray elastic scattering amplitude (f) are made using the crystallographic data from the literature and using the code ATOMS, which generates input files for the FEFF code [11].

4. Results and discussion

The theoretical EXAFS spectra of the three compounds: tetragonal zirconia, monoclinic zirconia, and hexagonal close-packed zirconium were first calculated using FEFF8 and using input from ATOMS and the data from Tables 1 and 2. These spectra are used as references. The 10 μm sample could be a mixture of both allotropic forms as observed by Yilmazbayhan et al. [12] using μXRD on Zry samples corroded in contact with water at 595 K. The authors note a substantial amount of tetragonal zirconia through the micron thick layer near the Zircaloy interface due to internal stresses between the phases. For this VIAXAS study, it must be noted that the penetration depth x that is a function of the incident angle ϕ may be estimated from Eq. (1) and $x = l_i \sin\varphi$. Consequently, the incident beam should reach for small angle and 90% absorption in zirconia depths of: 1 μm for 1°, 5 μm for 5° and 10 μm for 10°.

4.1. VIAXAFS spectra

Both XANES and EXAFS results are discussed in a comparative way in this Section using current

Table 1
Crystal structure of components from this study

Space group	m-ZrO_2	t-ZrO_2	hcp-Zr
	$P2_1/c$	$P4_2/nmc$	$P6_3/mmc$
a (pm)	514.6	364	323.2
b (pm)	521.3	364	323.2
c (pm)	531.1	527	514.7
α (°)	90.00	90.00	90.00
β (°)	99.23	90.00	90.00
γ (°)	90.00	90.00	120.0

Table 2
Atomic coordinates

Sites	m-ZrO_2	t-ZrO_2	hcp-Zr
x_{Zr}	0.276	0.75	0.00
y_{Zr}	0.041	0.25	0.00
z_{Zr}	0.208	0.75	0.00
x_{O1}	0.070	0.25	N/A
y_{O1}	0.336	0.25	N/A
z_{O1}	0.341	0.46	N/A
x_{O2}	0.442	N/A	N/A
y_{O2}	0.755	N/A	N/A
z_{O2}	0.479	N/A	N/A

N/A: non-applicable.

Table 3
E_0 values for the 10 μm ZrO_2/Zry sample

ϕ (°)	E_0 (keV)
0.10	18.004
0.25	18.001
3.00	17.998
10.0	17.999
20.0	17.999
30.0	17.999
40.0	17.998
50.0	17.999
60.0	17.999
70.0	17.999

Note: $E_0 = 17.998$ keV for Zr and $E_0 = 18.014$ keV for m-ZrO_2.

methodology [13]. At the zirconium K-edge energy, the X-ray beam may pass through the zirconia film, then into the Zircaloy matrix, the later contributing to the fluorescence intensity. Through VIAXAFS (see Fig. 3), it is expected that successive layer depths will exhibit the properties of the different constituents of the 10 μm film sample. E_0 was calculated using the two polynomial fit (1st deg, 2nd deg), and the E_0 values were determined by derivative tests. The values of E_0 are summarized in Table 3, from which the normalized absorption spectra are derived for the sample at various angles, as shown in Fig. 4. Clearly some signal from the metal matrix appears before the expected incident angle e.g. 10° for the 10 μm expected layer. This is due to the geometry of the system, the layer relief and the structure of the layer itself. Consequently some metal signal appears already at lower angles shifting locally the XAFS data toward lower energies (see

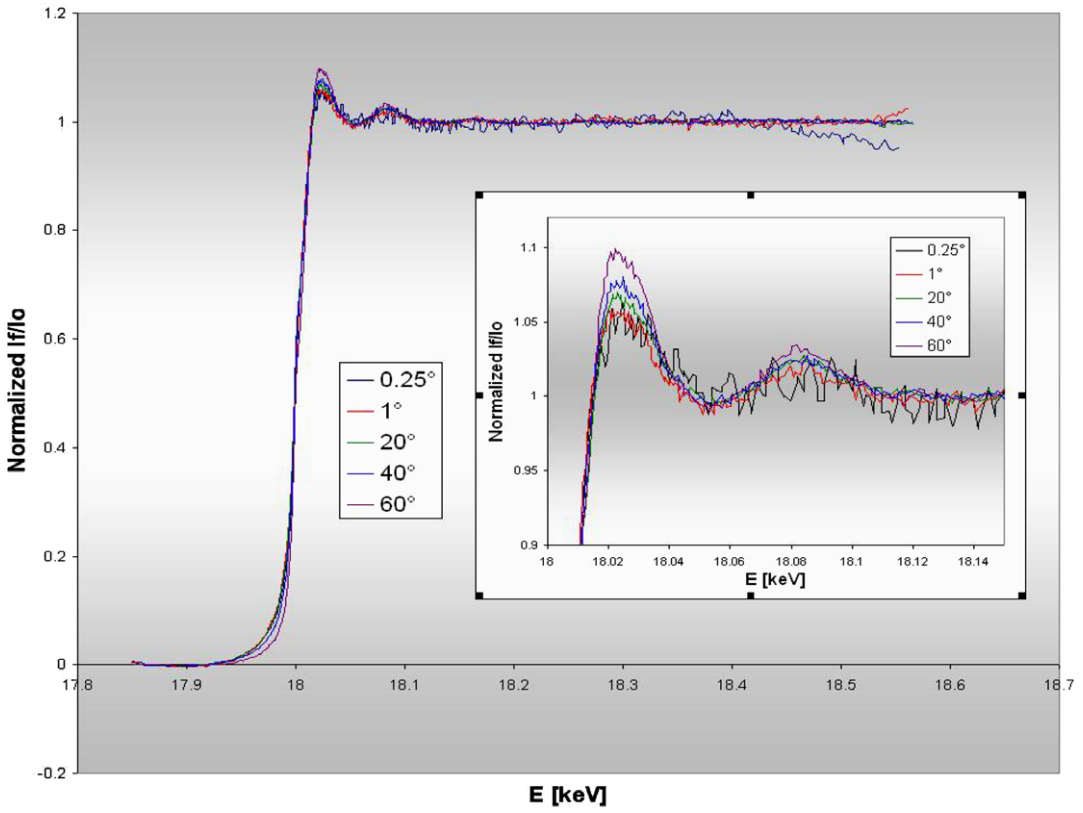

Fig. 3. XANES of the 10 μm ZrO2/Zry sample for various incidence angles.

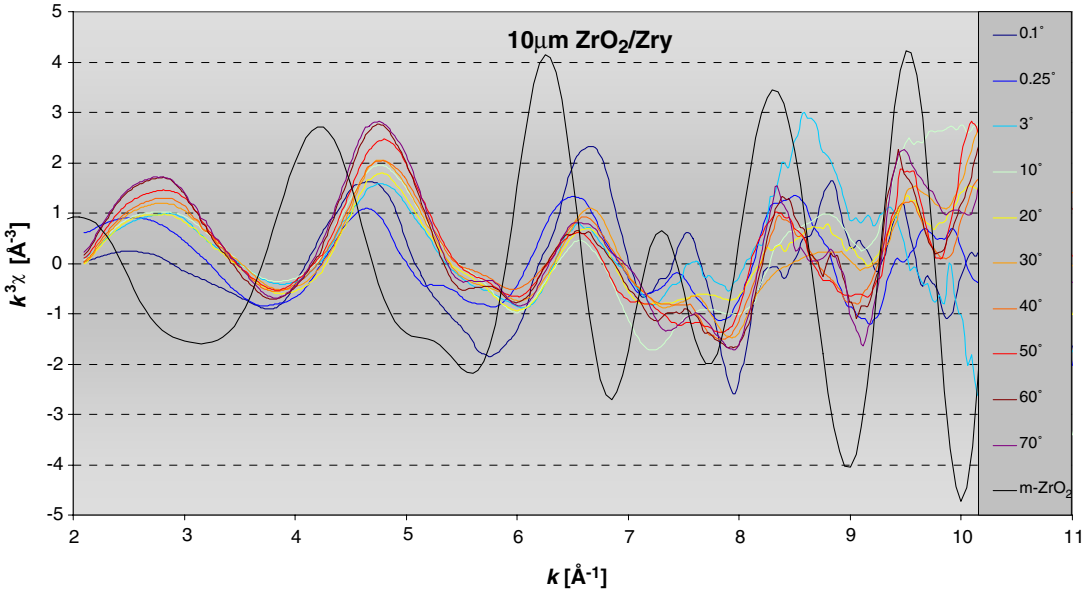

Fig. 4. k^3-weighted EXAFS spectra of 10 μm ZrO_2/Zry for various incidence angles and comparison with the FEFF calculated spectrum for *m*-ZrO_2.

Table 3). Comparison between the spectra at grazing incidence and those at higher incidence angles on the sample indicates a clear evolution of the white line, which is much stronger at larger angles.

As seen in Fig. 3 for the 10 μm ZrO_2/Zry sample, the GI spectra also exhibit a much higher signal to noise ratio than the spectra at larger angles, this may be due to the larger dispersion of the incident light on the sample and because the sample surfaces are not perfectly flat. As can be seen in the SEM images (Fig. 2), the sample shows a large density of microscopic bar crystals on its surface, reducing the 'average density' of the material at the surface. The density however increases within the layer thickness. Due to the surface relief, some of the absorbing atoms will not have the same number of next neighbours as the atoms within the sample [9]. Thus, for very small incidence angles, the XAFS spectra resemble more the spline absorption spectrum of the surface material.

4.2. Comparing the $k^3\chi$-EXAFS spectra

Information about material properties can be extracted from the χ-spectra by comparing them with theoretical spectra of known materials generated by FEFF simulation. In order to emphasize the fluctuations occurring at larger k ($k > 5$ Å^{-1}), the normalized spectra are weighted by a factor of k^3. The theoretical χ-spectra of the three compounds of interest were calculated. The EXAFS spectra were normalized using WinXAS. The values of E_0 summarized in Table 3 for the various measured angles were used to calculate the spectra. Fig. 4 depicts the k^3 weighted χ-spectra at various angles for the sample.

The 10 μm ZrO_2/Zry sample is expected to contain tetragonal and monoclinic zirconia on a zirconium substrate. It is also expected that the hcp zirconium will become detectable by VIAXAFS at higher angles. The sample is quite difficult to analyze because the zirconia thin film lies on a zirconium bed, the fluorescence detected photons could be produced by the zirconia film or by the zirconium bed, and in the zirconia film the fluorescence photons could be produced by the atoms in a monoclinic configuration or in a tetragonal configuration. As can also be seen in Table 3, there is an energy shift of ~5 eV occurring in the spectra of this sample. This is due to the decrease of E_0 as a function of the incident angle revealing the shift from a ZrO_2 pure signal to a signal involving a Zr metal component. For the other spectra, a clear evolution can be seen in the height of the first three maxima and in the turbulence at higher k. The most notable variation occurs between $7.0 < k < 8.5$. It is in this region that the influence of the tetragonal zirconia could be detected and the

influence of the hcp metal zirconium begins to be visible.

The shift between the experimental spectra and the m-ZrO_2 spectrum is some what significant. It may be estimated using Eq. (9) or $(E - E_0) = 3.81\ k^2$ (with E in eV and k in $Å^{-1}$) corresponding to a non-linear shift in the k space. Thus, a 10 eV E_0 drift (ΔE_0 as observed, see Table 3) induces k shifts ($\Delta k = (k^2 + \upsilon \cdot \Delta E_0)^{1/2}$ with $\upsilon^{-1} = 3.81$ eV $Å^2$) of $\sim 0.4\ Å^{-1}$ for the maxima at $4\ Å^{-1}$ and of $\sim 0.2\ Å^{-1}$ for the maxima at $6\ Å^{-1}$. On the other side, the zirconia layer is composed of millions of nano bar-crystals as reported [12]. Thus the defect density in the zirconia thin film is larger than in bulk monoclinic zirconia reducing the XAFS waves in the spectra (see [9]).

4.3. VIAXAFS depth profiling

The major modelling work of this study consisted of quantifying the spline functions for the different values of the spline absorption coefficients and intensities used in Eqs. (4)–(8): $\bar{\mu}_T(x), \bar{\mu}_a(x), \mu_f(x)$, and $\bar{I}(x)$. For a uniform ideal sample of a given material, the absorption coefficient is assumed to remain constant regardless of the incidence angle of the X-ray beam. The self-absorption correction has to be operated in order to compensate for the damping of the signal amplitude.

For the sample, the depth evolution may be supposed to be dependant on the density of the material, so the absorption coefficients can be written as $\mu(x) = \rho(x)\mu$. The density can be modelled as $\rho(x) = \rho(0)[1 - A \ \exp - (kx)]$ starting at $\rho(x) = 0.50$ for $x = 0.00$ μm and reaching $\rho(x) = 0.98$ at $x = 3$ μm with $A = 0.50$ and $k = 1.0 \times 10^6\ m^{-1}$ for the sample under investigation. Caution has to be made though as to the computation of ρ, particularly with regard to the integrated Eq. (3). In order for the form of the equation for the intensity to remain the same, the ρ factor has to be constant. Therefore, in the computation of $\bar{I}(x)$, the constant ρ that was used was a weighted average of $\rho(x)$ for the target depth $(x, x + \delta x)$. This approximation is adequate as long as the density/depth evolution is not too irregular and sharp. With the sample, as can be seen in Fig. 2(a), the surface shows random irregularities, thus producing a regular increase in sample density as the sample depth x increases. For the 10 μm ZrO_2 corrosion layer, however, the task is more complicated; the regular increase in density with depth has to be accounted for as well as the sudden transition from one zirconia to zirconium at $x = \sim 10$ μm. A superposition of terms appears in Eqs. (4) and (5) and (8) in order to express the entire absorption process. The values for the spline absorption coefficients $\bar{\mu}_T(x), \bar{\mu}_a(x), \mu_f(x)$ were extrapolated from virtual tables of material X-ray

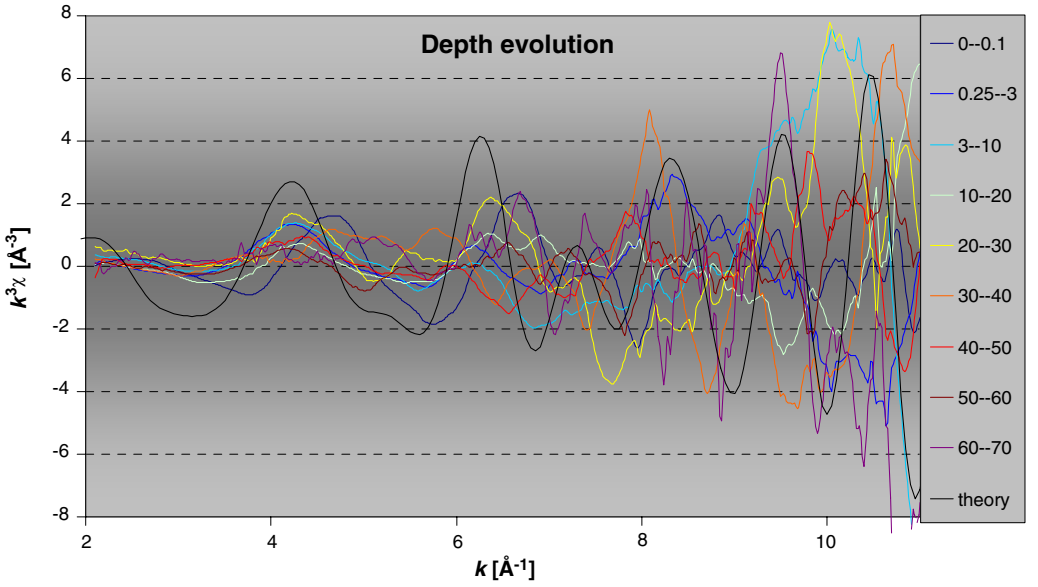

Fig. 5. Evolution of the k^3-weighted EXAFS spectra obtained by layer subtraction (angle values in °) through the 10 μm ZrO_2/Zry sample compared with the calculated FEFF spectrum for m-ZrO_2 (theory).

properties [14]. This was applied for the layer subtraction and VIAXAFS analysis was successful for the regions of depth analysis (see Fig. 5).

Fig. 5 presents the various k^3-weighted EXAFS spectra obtained by VIAXAFS analysis of the 10 μm ZrO_2/Zry sample. Clearly, zirconia is detected for shallow angles while zirconium metal is detected for larger incident angles. Note that the shift between the experimental spectra and the m-ZrO_2 spectrum is corrected except for 0–0.1° because it corresponds to the experimental spectrum recorded for $\varphi = 0.1^{\circ}$.

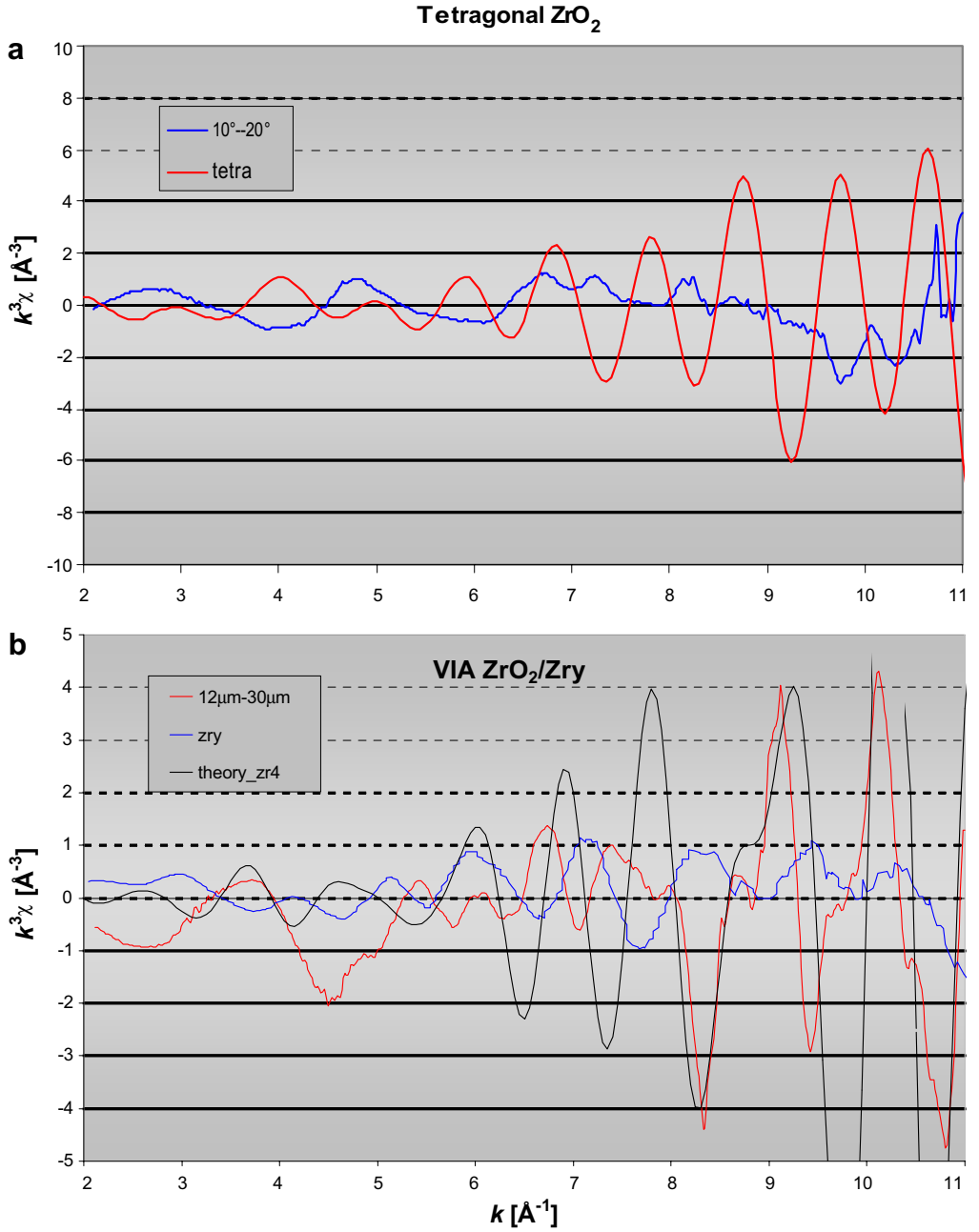

Fig. 6. (a) Comparison of theoretical tetragonal zirconia spectrum vs. VIAXAFS through layer (~7.5 to ~11.0 μm) of sample supposed to contain the tetragonal zirconia. (b) Detection of hexagonal close packed zirconium from the underlying metal matrix (~12 to ~30 μm) by VIAXAFS of the 10 μm ZrO_2/Zry sample.

The wave reduction due to the porous zirconia composition affects the spectra. XAFS analysis on the Zr K edge identifies a lower number of next neighbour Zr atoms in the corroded samples compared to the monoclinic crystal. This may be due to the density for given average atom distances suggesting a high density of dislocations and defects e.g. [8] as this has been reported earlier [12].

Fig. 6(a) isolates the layer of depth ~7.5 to ~11.0 μm in order to assess whether the presence of tetragonal zirconia is detectable within the target layer as suggested in the literature [11]. Here it can be stated that the fraction of tetragonal zirconia should be less than 10%. The general layer profiling is not very revealing of the internal structure of the material. The reason for this lack of success in VIAXAFS analysis can be attributed to either of the following facts: a lack of precision in the experimental data or a high signal to noise ratio.

The layer subtraction did indicate the presence of metal zirconium at the target depth (12–30 μm) as can be seen (Fig. 6(b)) in the resemblance between the theoretical zirconium spectrum and the isolated layer one at $k > 8$ Å^{-1}. The presence of zirconium deep in the sample is apparent only at large k because the monoclinic zirconia spectra and the metal zirconium are fairly similar for small k.

5. Conclusions and prescriptions for future development of VIAXAFS

The results obtained are satisfying in that they clearly indicated that the method of VIAXAFS is feasible for the analysis of corrosion layers. The VIAXAFS analysis on the 10 μm ZrO_2/Zry sample was quite difficult due to the complexity of the sample structure. The results from the Zr K edge spectra obtained in Figs. 4–6 do however indicate that the method has a great potential, even with complex samples. XAFS analysis suggests a lower number of next neighbour Zr atoms in the corroded sample than in the bulk oxide material. This may be due to the relative high density of dislocations and defects in the corrosion layer. The discussion underlines that the technique reveals nano-pores, dislocations, vacancies or defect features. The presence of tetragonal zirconia is not observed for zirconium alloy corrosion layers.

Several avenues have to be further developed in order to render the method more practical. For measurement processes, it would be necessary to automate the goniometry of the sample so that the sample pivots by the desired step ($\Delta\varphi$) automatically, without the need for constant supervision. Most importantly, in order to model and analyze the VIAXAFS data adequately, it is imperative to develop a software capable of integrating VIAXAFS parameters. These parameters are primarily: uniformity of normalization process, uniformity of k-step for manipulation of data on a spreadsheet, automatic generation of spline functions based on some basic parameters of the material composition (density, layer structure, beam penetration depth criteria, interface for $\rho(x)$ function estimate,...). Finally, an important subsequent analysis to make would be to estimate the required precision of spectra and background to noise ratio as a function of variable incidence step size.

Acknowledgments

Acknowledgements are due to Melissa Denecke and Jörg Rothe from the INE-ANKA beam line for their precious help in operating the line during the sample investigations. Thanks are due to Roland Brütsch at the PSI-LWV for his valuable SEM work and to Christian Hellwig head of the CMB program for his interest in this work. Thanks are also due to Johannes Bertsch, Annick Froideval, Goutam Kuri (LWV) and Rainer Dähn (LES) for their punctual interests. The VIAXAFS study was partially supported by swissnuclear.

References

[1] C.H. Booth, F. Bridges, Phys. Scr. Online T115 (2005) 202.
[2] P. Pfalzer, J.-P. Urbach, M. Klemm, S. Horn, Phys. Rev. B 60 (1999) 9335.
[3] L. Tröger, D. Arvanitis, K. Baberschke, H. Michaelis, U. Grimm, E. Zschech, Phys. Rev. B 46 (1992) 3283.
[4] M. Kastoriano, C. Degueldre, K. Dardenne, VIA-XAS for the study of zirconia films. PSI Internal Report: TM 43-05-23.
[5] C. Degueldre, A. Amato, G. Bart, J. Script. Mater. 54 (2005) 1211.
[6] C. Degueldre, T. Arima, Y.W. Lee, J. Nucl. Mater. 319 (2003) 6.
[7] P. Villela, S. Conradson, F. Espinosa-Faller, S.R. Foltyn, K.E. Sickafus, J.A. Valdez, C. Degueldre, Phys. Rev. B 64 (2001) 1041011.
[8] S. Conradson, C. Degueldre, F.J. Espinosa-Faller, S.R. Foltyn, K.E. Sickafus, J.A. Valdez, P.M. Villella, Progr. Nucl. Energy 38 (2001) 221.
[9] C. Degueldre, K. Dardenne, Nucl. Instrum. and Meth. B 238 (2005) 323.

[10] W.H. McMaster, N. Kerr Del Grande, J.H. Mallett, J.H. Hubbell, Compilation of X-ray Cross Sections, Lawrence Livermore National Laboratory, 1969.
[11] A.L. Ankudinov, B. Ravel, J.J. Rehr, S.D. Conradson, Phys. Rev. B 58 (1998) 7565.
[12] A. Yilmazbayhan, A.T. Motta, R.J. Comstock, G.P. Sabol, B. Lai, Z. Cai, J. Nucl. Mater. 324 (2004) 6.
[13] A. Gualtieri, P. Norby, J. Hanson, J. Hriljac, J. Appl. Crystallogr. 29 (1996) 707.
[14] W.H. McMaster, N. Kerr Del Grande, J.H. Mallett, J.H. Hubbell, Compilation of X-Ray Cross Sections, UCRL-50174 Section II Revision I, 1969.